Increasing Vertical Resolution and Updating Physical Processes in JMA's Regional NWP System

KUSABIRAKI Hiroshi*, KITAMURA Yuji, SAWADA Masahiro, MATSUBAYASHI Kengo, and NISHIMOTO Shusuke

Numerical Prediction Development Center, Japan Meteorological Agency
*Correspondence to: H. Kusabiraki, Numerical Prediction Development Center, 1-2 Nagamine, Tsukuba, Ibaraki 305-0052, Japan. E-mail: hiro.kusabiraki@met.kishou.go.jp

1 Introduction

A Local Forecast Model (LFM) is used to provide short-range forecasts for disaster mitigation and aviation safety as part of the JMA's operational regional NWP systems (JMA, 2019). This report provides a brief overview of an LFM upgrade from the previous version (LFM2003) to the new version (LFM2103), which went live on 31 March 2021.

2 Increased Vertical Resolution

LFM2003 employed hybrid terrain-following vertical coordinates with the lowest model level height of 20 m. In LFM2103, the number of vertical levels is increased from 58 to 76. The vertical coordinates of the new model have more levels in the Planetary Boundary Layer (PBL) than the old one, with a lowest model level height of 10 m. The increased vertical resolution of LFM2103 allows better representation of surface flux and subgrid turbulent mixing in the PBL.

3 Physics Updates

The various physical parameterisation developments in LFM2103 provide significant improvement in predictive skills over LFM2003 as outlined below.

3.1 Cloud Fraction

LFM2003 was affected by negative bias in Outgoing Longwave Radiation (OLR) in comparison to satellite observation as a result of upper-level cloud fraction overestimation. LFM2103's new cloud fraction scheme based on Wilson and Ballard (1999) reduces ice water content in mixed-phase cloud and ice cloud coverage, thereby reducing OLR biases.

3.2 Turbulent Mixing

The mixed subgrid scale (SGS) vertical transport scheme proposed by Moeng et al. (2010) was introduced in LFM2103. In this scheme, the vertical SGS fluxes are represented by an LFM PBL scheme and a modified Leonard term given by

$$L_{\phi w} = \frac{K_L}{12}\left(\Delta_x^2 \frac{\partial \bar{\phi}}{\partial x}\frac{\partial \bar{w}}{\partial x} + \Delta_y^2 \frac{\partial \bar{\phi}}{\partial y}\frac{\partial \bar{w}}{\partial y}\right), \qquad (1)$$

where Δ_x and Δ_y represent horizontal grid spacing of 2 km, $\bar{\phi}$ represents grid scale variables such as potential temperature and specific humidity, and $\bar{w}$ represents grid scale vertical velocity. K_L is set as 4 based on Verrelle et al. (2017). The Leonard term represents unresolved vertical transport of heat and moisture in deep convection. Figure 1 shows an example of the Leonard term simulated in two-dimensional (2D) idealised deep convection. Upward SGS heat fluxes based on the Leonard term ($L_{\theta w}$, where θ is potential temperature) are represented adjacent to the updraught peak, resulting in reduced grid scale vertical transport.

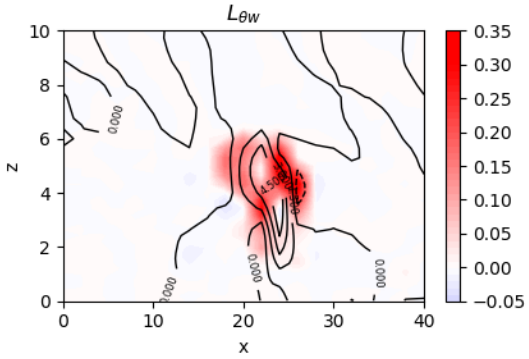

Figure 1: 2D simulation of the Leonard term for potential temperature (K m s^{-1}) given by Eq. (1) based on idealised deep convection with atmospheric profiles initialised in a TRMM-LBA experiment. Black lines denote vertical velocity (m s^{-1}).

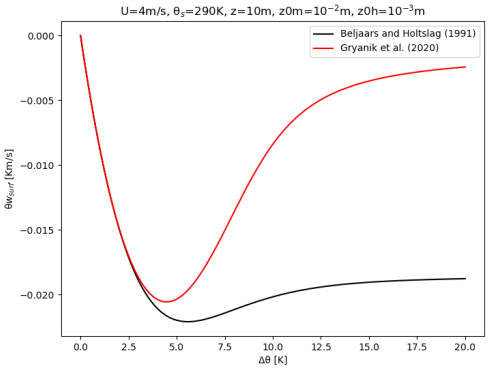

Figure 2: Surface heat flux calculated using the stability functions of Beljaars and Holtslag (1991) (black lines) and Gryanik et al. (2020) (red lines) in a stable boundary layer. The horizontal axis denotes potential temperature differences between the lowest model level and the surface.

3.3 Surface fluxes

In LFM2003, stability functions proposed by Beljaars and Holtslag (1991) (BH91) were used in both stable and unstable boundary layers. For stable

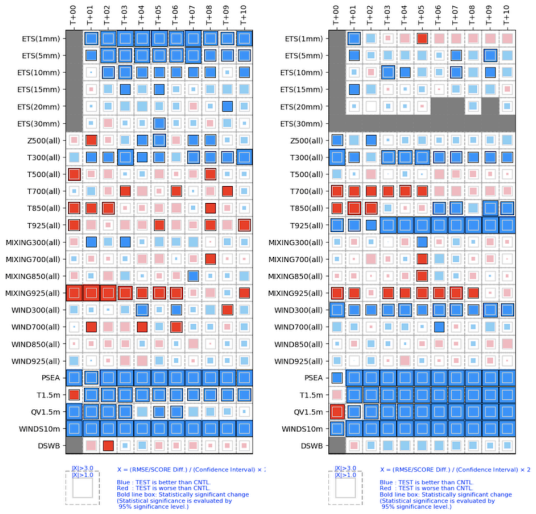

Figure 3: Score difference between LFM2103 and LFM2003 with verification against precipitation based on radar/raingauge precipitation analysis, and synoptic and radiosonde series observation from the experiments conducted in summer (27 June to 8 July 2018; left) and winter (16 January to 27 January 2018; right). Rows represent ETS and RMSE differences for particular parameters, and columns represent forecast ranges from initial to 10 h (T+10). Blue boxes represent increased (reduced) ETS (RMSE) (i.e., improvement), whilst red boxes represent degradation. The area of filled boxes denotes significance, and solid outlines denote statistically significant differences.

boundary layers (SBLs) in LFM2103, the function proposed by Gryanik et al. (2020) (GLGS) was adopted. Figure 2 shows fluxes diagnosed with the stability functions of BH91 and GLGS in an SBL. The GLGS scheme reduces downward heat transport as compared to BH91, thereby mitigating excessive cooling of near-surface air in the SBL.

3.4 Land surface

Ancillary data related to land-surface properties were also significantly changed from the source data used in LFM2103. (i) Thermal roughness lengths over urban surfaces were reduced based on Kanda et al. (2005), and (ii) land surface albedo climatology was updated based on the MODIS Terra and Aqua gap-filled snow-free product. For (ii), most land-surface areas in LFM2103 are darker than those in LFM2003, and (i) and (ii) together achieve a better diurnal cycle for surface temperature. The new model incorporates a subgrid vegetation cover fraction (VCF) supporting accurate latent heat fluxes over non-vegetation surfaces. The maximum green vegetation fraction product developed by Broxton et al. (2014) was applied as the VCF for LFM2103.

4 Evaluation

Figure 3 summarizes the differences in equitable threat scores (ETSs) and root-mean-square errors (RMSEs) between LFM2103 and LFM2003 from NWP forecast skill evaluation. The ETS for rainfall amounts was calculated against radar/raingauge-analysed precipitation, and the RMSE for each field was calculated against synoptic surface and radiosonde observations. Significant improvement in precipitation and near-surface diagnostics is observed, especially for 1.5-m temperature and 10-m wind speed. There are also improvements to temperature at 300 hPa, primarily due to reduced ice cloud fractions. The degradation of lower atmospheric humidity in summer from overestimation of moisture fluxes over the ocean and semi-arid regions in China needs to be tackled in future configurations.

References

Beljaars, A. C. M. and A. A. M. Holtslag, 1991: Flux Parameterization over Land Surfaces for Atmospheric Models. *J. Appl. Meteor. Climat.*, **30**, 327–341.

Broxton, P. D., X. Zeng, W. Scheftic, and P. A. Troch, 2014: A MODIS-Based 1 km Maximum Green Vegetation Fraction Dataset. *J. Appl. Meteor. Climat.*, **53**, 1996–2004.

Gryanik, V. M., C. Lüpkes, A. Grachev, and D. Sidorenko, 2020: New Modified and Extended Stability Functions for the Stable Boundary Layer based on SHEBA and Parametrizations of Bulk Transfer Coefficients for Climate Models. *J. Atmos. Sci.*, **77**, 2687–2716.

JMA, 2019: Outline of the operational numerical wether prediction at the Japan Meteorological Agency. [Available online at `https://www.jma.go.jp/jma/jma-eng/jma-center/nwp/outline2019-nwp/index.htm`].

Kanda, M., T. Kawai, M. Kanega, R. Moriwaki, K. Narita, and A. Hagishima, 2005: A Simple Energy Balance Model for Regular Building Arrays. *Bound.-Layer Meteor.*, **116**, 1573–1472.

Moeng, C.-H., P. P. Sullivan, M. F. Khairoutdinov, and D. A. Randall, 2010: A Mixed Scheme for Subgrid-Scale Fluxes in Cloud-Resolving Models. *J. Atmos. Sci.*, **67**, 3692–3705.

Verrelle, A., D. Ricard, and C. Lac, 2017: Evaluation and Improvement of Turbulence Parameterization inside Deep Convective Clouds at Kilometer-Scale Resolution. *Mon. Wea. Rev.*, **145**, 3947–3967.

Wilson, D. R. and S. P. Ballard, 1999: A microphysically based precipitation scheme for the UK meteorological office unified model. **125**, 1607–1636.